submitted to *Geophys. J. Int.*

Reciprocal error in Time Domain Induced Polarization: Systematic Noise or Systematic Signal?

L. Vanhooren[1,2⋆], W. Deleersnyder[1], A. Flores-Orozco[3], F. Nguyen[4], C. Caudron[2], T. Hermans[1]

[1] *Laboratory of Applied Geology and Hydrogeology, Ghent University, Belgium.*

[2] *G-Time laboratory, Université libre de Bruxelles, Belgium.*

[3] *Department of Geodesy and Geoinformation, TU-Wien, Austria.*

[4] *Urban and Environmental Engineering, ULiege, Belgium.*

June 22, 2026

SUMMARY

Reciprocal measurements are standard for data quality control in electrical resistivity surveys, but their potential as an interpretation tool is rarely exploited. Under the assumption of linear subsurface behaviour, normal and reciprocal readings should yield the same results, but when a systematic offset is present it can be indicative for additional processes. Here we present a time-domain induced polarization (TDIP) dataset from a volcanic hydrothermal system (Reykjanes, Iceland) where a strong, systematic offset between normal and reciprocal measurements is observed. The discrepancy is present as a positive shift of the reciprocal decay curves (>100 mV/V). While both normal and reciprocal inversions resolve a strong IP anomaly in the southern part of the profile, a substantial offset exists between the two (>20 mS/m). The offset is spatially confined and persistent over 100 consecutive days, the anomaly itself coincides with a strong IP response attributed to the mutual occurrence of clay minerals and disseminated iron sulphides and oxides. Besides random noise, we evaluate four possible mechanisms for the offset: (1) polarization of the electrodes, (2) inherent sensitivity differences between normal and reciprocal configurations, (3) stray currents from the nearby powerplant and (4) nonlinear IP effects where the response depends on the current density. Given the geological context and the localized nature of anomaly, a non-linear effect is plausible but the ambiguity between systematic noise and a genuine subsurface signal cannot be fully resolved with field data alone. This study demonstrates that the systematic analysis of normal-reciprocal misfit in TDIP can serve as a widely accessible tool for identifying signals that, whether geologic, or anthropogenic in origin, are overlooked by standard data quality workflows.

Key words: reciprocal discrepancy – induced polarization – volcanic hydrothermal systems – non-linearity

1 INTRODUCTION

Induced polarization (IP) is a geo-electric method that characterizes the ability of the subsurface to temporarily polarize electrical charges under an applied electrical current. IP is usually expressed by the resistivity and chargeability or, by the real and imaginary components of the complex conductivity, with the imaginary component and the chargeability being linearly related given a constant phase-angle (Binley & Slater, 2020). It is sensitive to the presence of (semi-) conductive minerals (Pelton et al., 1978), certain clays (Lévy et al., 2018), and pore-space geometry (Weller et al., 2016). In environments where bulk electrical parameters can be caused by different processes (for example, low resistivity can be caused by clays and/or high salinity), IP can further distinguish between the source of the signals. Hence, IP is often preferred in complex environments over the more traditional DC-methods like Electrical Resistivity Tomography (ERT) (Slater & Lesmes, 2002; Cong-Thi et al., 2024). The IP method has proven effective in detecting (semi-) conductive minerals such as magnetite and pyrite (e.g. Flores-Orozco et al., 2011; Flores Orozco et al., 2013), thus, it has gained popularity in volcanological studies (Ghorbani et al., 2018). IP has also been applied to characterize fracture networks, influencing local flow patterns and degassing regime (Troiano et al., 2021), to map the extent of hydrothermal alterations (e.g. Revil et al., 2002; Vanhooren et al., 2025), and to detect CO_2 rich groundwater (Defourny et al., 2020).

The principle of reciprocity states that, in a geo-electric survey, when current and potential

⋆ Lore.Vanhooren@UGent.be

dipoles are interchanged, the readings should yield the same result, given a homogeneous, source-free, and linear character of the subsurface (Parasnis, 1988). The collection of reciprocals is common practice in ERT surveys to assess data quality (Slater et al., 2000; Vanhooren et al., 2025), as a result, they are often available in TDIP surveys but they remain largely unused as TDIP requires more detailed processing methods (Flores Orozco et al., 2018). Commonly, the discrepancies between normal and reciprocal settings are caused by random noise and thus distributed according to a Gaussian distribution (LaBrecque et al., 1996). When discrepancies are spatially confined, it is indicative of additional processes. In this contribution, we consider measurement errors, systematic noise caused by stray currents, and non-linearity as possible origins for the discrepancies in this IP dataset. The first can be overcome by careful survey design (Dahlin et al., 2002), but distinguishing between the latter two is not straightforward, as we illustrate here.

It is often assumed for simplicity that the electrical properties exhibit linear behaviour (Pelton et al., 1978), i.e. that they are independent from the potential difference. This linearity is at the heart of the reciprocity theorem (Parasnis, 1988). However, under specific subsurface and measurement circumstances, non-linearity can exist, several mechanisms for non-linear induced polarization (NLIP) have been proposed. At the interface of (semi-) conductive minerals and the electrolyte, the charge-transfer kinetics described by the Butler-Volmer equation can move into the non-linear domain at elevated potential, producing harmonic distortions in the signal (Klein & Shuey, 1978a,b). Ion exchange at the surface of clays and zeolites can also produce non-linear responses (Olhoeft, 1979) but the process is less well documented and the magnitude of the contribution is uncertain. It was proposed that the effect could be amplified by the interaction with organic contaminants (Olhoeft, 1985) tough more recent studies contest this, linking the effect poor experiment design (Ustra et al., 2012, e.g.). More recently, Hallbauer-Zadorozhnaya et al. (2015, 2016) demonstrated that the process of membrane polarization is inherently non-linear. Under elevated current density, the concentration gradients across pore constrictions become large enough that the back-current, which drives the polarization, no longer scales linearly with the applied field, causing both resistivity and chargeability to become dependant on the current density.

A common requirement in these mechanisms is the need of a significantly large current density or potential, which are rarely attained in field conditions with traditional equipment, where current densities are orders of magnitude lower than the densities at which non-linearity was demonstrated in the laboratory (1-10 mA/cm²) (Klein & Shuey, 1978a; Florsch et al., 2026). The current distribution considered in a geoelectic survey is in reality a homogeneous average, on the grain-scale heterogeneities in the mineral assemblage can cause heterogeneous and irregular current distribution, characterized by local maxima, a process well known from effective medium theory (Snarskii et al., 2019; Zhdanov, 2008). In these areas the local current density can exceed the threshold needed to move into the non-linear behaviour, even when the bulk current density remains low. Methods to detect NLIP typically rely on the spectral analysis of the harmonic distortion (Olhoeft, 1979; Bigalke & Junge, 1999). Field deployment of IP is often done in the time domain, using commercially available instruments, making the spectral approach less accessible for routine surveys. Hallbauer-Zadorozhnaya et al. (2015, 2016) propose variable density profiling where repeated measurements are performed using different current densities, to identify areas of non-linearity. In their field case both resistivity and chargeability differ for varying current densities, albeit with the opposite sign, i.e, a decrease in resistivity and an increase in chargeability.

Here we impose different current densities by measuring reciprocals for a multigradient protocol, because the reciprocal setting will inject between a short dipole distance and measure between a long dipole, the current density will be inherently different than the normal setting. Notwithstanding, this will also cause differences in signal strength and sensitivity which have to be taken into account. In this contribution, we present a time-domain induced polarization dataset acquired as part of a continuous monitoring experiment in an active volcanic hydrothermal system aimed to detect changes in hydrothermal activity. The normal and reciprocal measurements exhibit a spatially focussed, systematic offset, the origin of which is investigated here.

2 MATERIALS AND METHODS

2.1 Complex Conductivity

The complex conductivity (σ^*) is a measure of the electrical properties of the subsurface. It is given by its real (σ') and imaginary (σ'') parts where the real part corresponds to the conduction strength or electromigration properties. The imaginary part represents the temporal, reversible energy storage, or polarization (Binley & Slater, 2020) hence the term induced polarization (IP). The complex conductivity σ^* can also be represented in terms of the magnitude $|\sigma|$ and phase shift φ, referring to the tangent of the real and imaginary components, and can thus be written as:

$$\sigma^* = |\sigma|e^{i\varphi} = \sigma' + i\sigma'' \tag{1}$$

and

$$\sigma' = |\sigma|cos\varphi, \tag{2}$$

$$\sigma'' = |\sigma|sin\varphi. \tag{3}$$

In porous media, in the absence of electronic conductors, the conduction is controlled by electrolytic and surface conductivity. The former is described by Archie's law (Archie, 1941) and is proportional to the fluid conductivity, saturation and pore space geometry, i.e. the total porosity and connectivity of the pore space. The surface conductivity is controlled by surface charges and specific area. This effect cannot be neglected in environments rich in fine materials (e.g. clay, silt, graphite), metals or organic materials (Flores-Orozco et al., 2011). Hence Archie's law warrants an extra term and can be generalized as the following (Waxman & Smits, 1968):

$$\sigma_b = \frac{1}{F}S^n(\sigma_w + B(\sigma_w)Q_v), \tag{4}$$

Stating the relationship between bulk conductivity σ_b and its different components, with: σ_w the water conductivity, S the saturation, n the saturation exponent, and F the formation factor accounting for the pore space geometry. The cation exchange capacity (CEC) is represented by two terms: the equivalent conductance of the cations $B(\sigma_w)$, and the cation-exchange per volume Q_v.

The presence of polarizable material complicates the interpretation, since the polarization of charge can be controlled by multiple mechanisms. In porous media, the most common one is related to diffusion-controlled polarization in the electrical double layer (EDL) due to the formation of local charge gradients. Two mechanisms drive the creation of such gradients, (1) blockage of ions in pore throats leading to a localized access of ions (membrane polarization); (2) the displacement of counter-ions in the Stern layer at mineral surfaces (Stern layer polarization), which is more abundant in minerals with a large surface area such as clays. The complex conductivity arising from the EDL polarization is strongly influenced by the conductivity of the pore fluid. At low salinity, the imaginary conductivity increases with increasing salinity until it reaches a plateau. At very high salinity, a drop in σ'' is reported due to the reduction in ion mobility in the EDL (Lesmes & Frye, 2001; Weller et al., 2015).

A second polarization type, electrode polarization, arises from the interaction of metallic minerals with an electrolytic fluid where the strong phase response is the result of a difference in transport rate between the ions (elecrolytic fluid) and electrons (metallic grain). Correlations have been reported between the strength of the phase response or imaginary conductivity and the volume of metallic minerals (Pelton et al., 1978; Slater et al., 2005; Revil et al., 2015). Polarization due to metallic minerals characteristically yields stronger responses in terms of apparent chargeability or phase shift than non-conductors (Revil et al., 2015).

2.2 Study Area

The study area is located on the Reykjanes Peninsula, Iceland, which has been volcanically active again since 2021. Based on historical data and recent events, six volcanic systems have been identified (Sæmundsson et al., 2020), not all of them host an active volcano, but can be geothermally active with an old magma intrusion as the heat source. This is the case for our study area, the Reykjanes system, hosting a high-temperature geothermal field of < 1km². Field operator HSOrka commissioned a 100MWe powerplant in 2006 for the production of electricity and warm water (Fridleifsson et al., 2020). Reservoir temperatures reach between 250°C and 300°C at a few 100 meters depth (Fowler et al., 2015) and more than 300°C between 1 and 2.5 km deep (Kadko et al., 2007). Because of the proximity to the ocean, the hydrothermal system is 100 % recharged by seawater (Kadko et al., 2007), which does not exclude the fact that a small (≈30 m) freshwater lens develops due to infiltrating rainwater (Sigurdsson, 1986). Host rocks are young, highly permeable basalts (Björnsson et al., 1970) that exhibit a traditional progressive hydrothermal alteration with depth (Marks et al., 2010).

The deep electrical conductivity signature of the field has been studied for the exploration of the geothermal system using transient electromagnetic (TEM) and magnetotelluric (MT) soundings (Karlsdottir et al., 2020), and controlled source electromagnetic (CSEM) measurements (Bretaudeau et al., 2021). Both studies confirm the presence of a low resistivity cap (1-3 Ωm), with an irregular geometry reaching the surface in the hot spring area and dipping down radially towards 1 km depth. The cap is underlain by a high resistivity core (10-100 Ω), characteristic for a geothermal field. High levels of heterogeneity have been reported in the shallow layer ($<$ 200m) (Karlsdottir et al., 2020). A shallow electrical resistivity tomography (ERT) survey, supported by induced polarization (IP), and self-potential (SP) show the types of heterogeneity (Vanhooren et al., 2025). The complexity of the shallow system is reflected by different types of surface manifestations corresponding to different geophysical signals: (1) Areas with intense surface alteration, such as mud pools and high local temperature gradients (6°C/cm), are characterized by a low resistivity signal ($<$ 5 Ohm.m) and a weak normalized chargeability ($<$ 3 mS / m), mainly caused by the presence of clays. (2) Part of the area is characterized by a shallow sealing structure in the upper 10 m, here the resistivity signature is low (<5 Ohm.m) but the normalized chargeability is higher (8-10 mS/m), the presence of the seal impedes movement of geothermal fluids to the surface, as a result no surface alteration is observed. (3) The majority of the site has no visible alteration on the surface or geophysical indications for alteration in the subsurface and are characterized by a high resistivity ($<$ 500 Ohm.m) and the absence of signal in normalized chargeability. However, other geothermal expressions can be possible, such as steam vents, which typically have a positive self potential anomaly caused by upflow of hydrothermal fluids. This highly variable resistivity distribution is controlled by local fractures and fluid flow patterns, where preferential pathways cause more progressive alteration Vanhooren et al., 2025, which is also observed by irregular, localized degassing patterns (Fridriksson et al., 2006).

2.3 Data acquisition and processing

2.3.1 Field Experiment

A permanent ERT / TDIP monitoring profile was installed at a location with highly variable hydrothermal activity (Hermans et al., 2026). The monitoring profile is 355m long, consisting of 72 stainless steel electrodes, with a spacing of 5m. Measurements are made using a *Syscal Pro* from IRIS instruments, with the *Syscal Monitoring Unit* to facilitate remote operation for monitoring. A square wave is injected using a 50% duty cycle and a pulse length of 1 s. For the chargeability measurements, after a delay of 40 ms, the voltage is measured in 20 semi-logarithmically ordered windows. The semi-logarithmic scheme was chosen because the time-windows are closer together in the first part of the decay, with a higher signal-to-noise ratio, and spaced further apart with lower S/N. Time windows 1-8 are measured every 20 ms, 9-14 every 40 ms, and 15-20 every 80 ms. Measurements are acquired using the multi-gradient protocol, with a normal protocol consisting of 1624 quadrupoles, while 2758 are collected in the reciprocal. The extra quadrupoles in the reciprocal are needed to make optimal use of the 10-channel system. The protocols were sorted to minimize electrode polarization effects, i.e., an electrode is never used for potential measurements just after having been used for current injection (Dahlin et al., 2002). Note that the monitoring survey was designed to monitor changes in the state of the hydrothermal system. As a consequence, survey design choices were made to maximize dense data acquisition for long periods without the need for human interventions.

2.3.2 Pre-Processing

Due to the high salinity (3.5 wt%) in the field , (Sigurdsson, 1986), the signal-to-noise ratio for the TDIP data is low (Vanhooren et al., 2025). The normal-reciprocal discrepancy between integrated chargeability is not suitable for filtering TDIP data since it cannot sufficiently identify outliers and readings with poor S/N ratios (Binley & Slater, 2020). More appropriate methods include a detailed analysis of the individual decay curves (e.g. Flores Orozco et al., 2018; Evrard et al., 2018). Here, we assess the quality of the curves by fitting a decaying exponential function and calculating the root-mean-square error (RMSE) with the observed data. Curves with an RMSE below

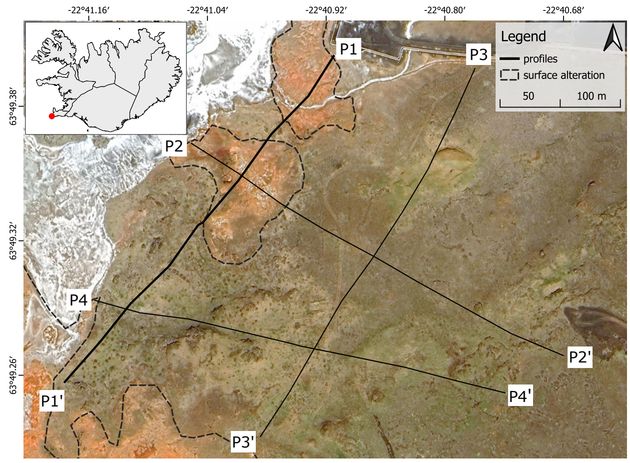

Figure 1. Location of the ERT/TDIP profiles (Vanhooren et al., 2025), profile 1 is the monitoring line. Profiles are measured form North to South and West to East, as indicated by the labels. The field area is indicated on the map of Iceland by the red dot.

75% are removed from the data, as well as non-decaying and negative curves. Curves decaying towards a non-zero value are sometimes removed as well (Evrard et al., 2018); however, here we retained them in the analysis as the discrepancy between normal and reciprocal emerges within these measurements, as we discuss below. Note that more advanced methods exist for data filtering, accounting for the spatial variability of the decay curves (Flores Orozco et al., 2018). However, their application requires spatially coherent chargeability values across the pseudosection to define meaningful reference curves. In our dataset, the presence of a localized offset between normal and reciprocal readings would violate this assumption, and the low signal-to-noise ratio inherent to the high-salinity environment would hinder the construction of representative reference curves. Given the already high rejection rate (62%) (Vanhooren et al., 2025), we opted for a less conservative, RMSE-based filter that retains the anomalous decays where the misfit is observed.

2.3.3 Inversion

Inversion is done using CRTomo (Kemna, 2000), solving the smoothness constrained regularized inversion using a Gauss-Newton iterative approach in terms of complex resistivity ρ^*, the inverse of σ^*. The calculations are expressed in terms of resistivity amplitude and the phase shift φ eq (1). In order to prepare the data for inversion, the chargeability obtained from TDIP measurement are linearly converted to phase shift in the frequency domain, relying on a constant phase angle response (CPA), (Kemna, 2000):

$$\rho^*{}_{CPA} = K(i\omega)^{-b} \quad (5)$$

Where K is a constant, i the imaginary unit, ω the angular frequency, and b a positive fractional exponent. The phase shift is given by $\varphi = -b\pi/2$ and defines the IP response (Lajaunie et al., 2016). The CPA model reduces the spectral IP response to two parameters (amplitude and phase), whereas the Cole-Cole model requires four parameters (resistivity, chargeability, the time constant and a frequency exponent) to capture the full spectral behaviour (Pelton et al., 1978). By converting the TDIP decay curves to a single phase value under the CPA assumption, the information is reduced to a single parameter per quadrupole. This simplification reduces the degrees of freedom in the inversion, at the cost of discarding any spectral information in the data (Lajaunie et al., 2016), notwithstanding the CPA model is widely adopted for field scale imaging (Evrard et al., 2018; Thibaut et al., 2021).

We chose to visualize the results in terms of complex conductivity with its real and imaginary parts, eqs (2)-(3). The regularized inversion can be further constrained by including prior information in the form of a reference model (Caterina et al., 2014). Care should be taken in the choice of the reference model as it introduces some subjectivity in the inversion (Oldenburg & Li, 1994). Here, we use a homogeneous reference model with a resistivity of 1 Ωm and a phase of 0 mrad. The closeness factor, weighing the importance of each cell (Hermans, 2014), is 0.01. Assessing the quality of the inversion is done using the cumulative sensitivity matrix (Kemna, 2000) and is representative of how well the data is resolved in the final model (Paepen et al., 2022). The two datasets (normal and reciprocal) are processed independently, using the same filtering criteria and inversion parameters. For the resistances, a linear error model was fitted giving an absolute error of 0.001 Ohm and 1.25 %, and a constant error of 5mrad is used for the phase inversion, for more detail on the inversion, we refer to Vanhooren2025. In order to appropriately assess the difference between the normal and reciprocal inversion, the additional points are removed from the reciprocal so the two datasets contain the same quadrupoles, where each quadrupole has a reading in the normal and reciprocal.

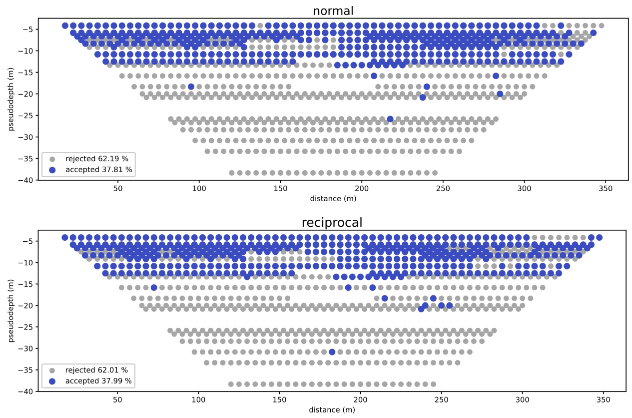

Figure 2. Pseudosections showing quadrupoles accepted (blue) and rejected (grey) after decay curve analysis, for both normal and reciprocal settings.

3 RESULTS

3.1 Chargeability signal

Decay curve analysis removes 62 % of the data in both normal and reciprocal datasets. In both cases, almost no data is retained below a pseudo-depth of 15 m (Fig. 2). This high rejection rate is expected, given the hydrogeology of the study site. The majority of rejected data are situated at depths at which the salinity of groundwater is high, where the decay times are too short to be measurable or the high ionic concentration prohibits the mobilization of ions necessary for polarization (Revil & Skold, 2011; Weller et al., 2015). The difference between the normal and reciprocal profile is best illustrated by the apparent resistivity and chargeability (Fig. 3a, b), where for each quadrupole the reciprocal is plotted against the normal. In theory, the points should plot on the 1:1 line if reciprocity conditions are respected, with some spreading related to noise. The apparent resistivity, shown in the logspace, has a good fit with values between 0.0001 and 350 Ωm, outliers are concentrated in the lower resistivity values. The case is different for the apparent chargeability, where a significant portion of the data has extreme values in the reciprocal data set ($>$ 200 mV/V), this trend is also present in the normal data, but less pronounced. In both cases, data is clustered around the axes, emphasizing the large reciprocal discrepancy; the reciprocity assumptions do not hold here.

To characterize the reciprocal discrepancy, we first examine the offset distribution of the resistivity and chargeablity data (Fig. 3c, d). While the overall distribution is centered around zero, a

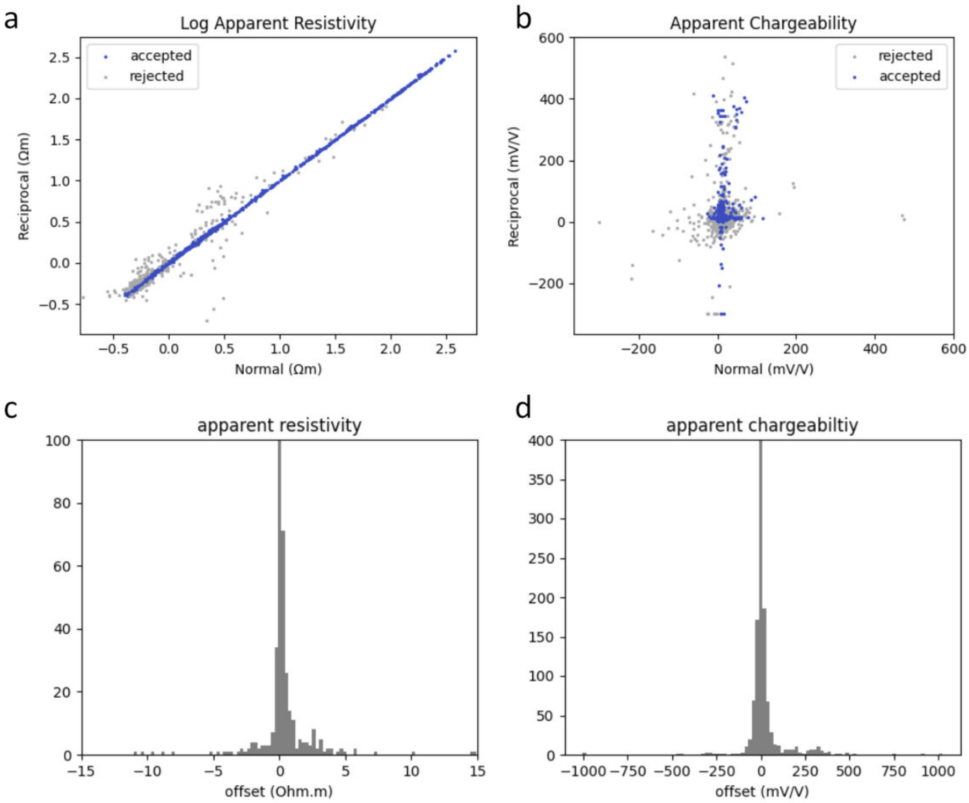

Figure 3. Reciprocal misfit for both resistivity and chargeablitiy data. The upper panels show a direct comparison of the normal vs. reciprocal, the lower panels display the corresponding offset distribution.

long tail of large offsets is visible for both data types but is more prominent in the chargeablity. The large discrepancies are difficult to resolve on a linear scale, to better visualize this tail, a symmetrical log-transform is applied (Fig. 4a). In a perfectly symmetrical distribution, both halves of the log-transformed plot would mirror each other, instead a secondary peak emerges between 100 and 550 mV/V on the positive side, with a subtle but corresponding increase between -100 and -500 mV/V on the negative side. We therefor adopt 100 mV/V as a threshold for a significant reciprocal offset.

The spatial organization of these discrepancies is presented in Figure 4b, which displays the chargeability offset for each pseudosection point. A positive value indicates a higher apparent chargeability in the reciprocal measurement, while a negative value reflects a higher measurement in the normal configuration. The pseudosection is restricted to a depth of -15 m, as data points beyond this were filtered out due to low signal to noise ratios. Two primary features can be resolved in the spatial distribution: an elongated pattern with a high negative offset ($<$ -100 mv/V) at the

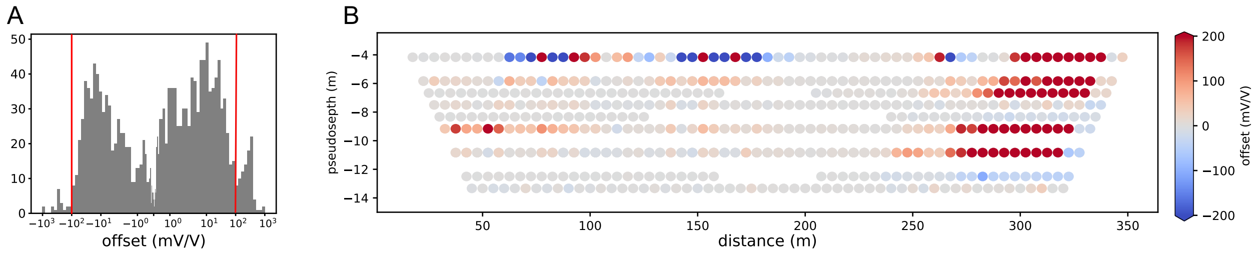

Figure 4. A) logarithmic distribution of the chargeability offset ($M_R - M_N$), an arbitrary cut-off of 100 mV/V is defined. B)Spatial representation of the chargeability offset between normal and reciprocal. The pseudosection was cut off at -15 m depth to coincide with the S/N threshold (Fig. 2)

shallowest depth level (-4 m) between 80 and 180 m, and a prominent cluster with a high positive offset ($>$ 100 mV/V) between 280 and 340 m. This second cluster, where the high chargeability population is concentrated, corresponds to the location of a shallow, hydrothermal seal (Vanhooren et al., 2025).

The offset between normal and reciprocal decays is further classified in three categories: a significant positive offset ($>$100 mV/V), a significant negative offset ($<$-100 mV/V), and a zero or minimal offset (between -1 and 1 mV/V) (Fig. 5). The majority of points that exhibit a large offset are positive, and account for 6.22 % of the data, both normal and reciprocal decay curves (Fig. 5A-C) have a clean-decaying character, but the reciprocal decay is not completely captured. Categorizing it as a decay towards a non-zero value is not appropriate since the voltage does not stabilize; hence, we consider these decays as incomplete. Points with a large negative offset account for a smaller fraction of the data (1.31 %), and can have the same behaviour as the category above but where the normal is shifted positively from the reciprocal (Fig. 5D), but in most cases they contain increasing reciprocals (Fig. 5E, F). This is well known as the negative IP effect and arises from the sensitivity distribution associated with the measurement protocol (Dahlin & Zhou, 2004). For a multigradient array, these effects are mostly present in the shallow layer, as is the case here. Lastly, a significant portion of the data has a near-zero offset between normal and reciprocal (Fig. 5 G-I), here arbitrarily set as 1 mV/V and accounting for 33.03 % of the data. The remainder of the data has a median offset, and is mostly transitional between the large and small offset.

When considering this offset in a context of nonlinearity, the current density is an important factor. Normal and reciprocal measurements of the multigradient array will inherently yield dif-

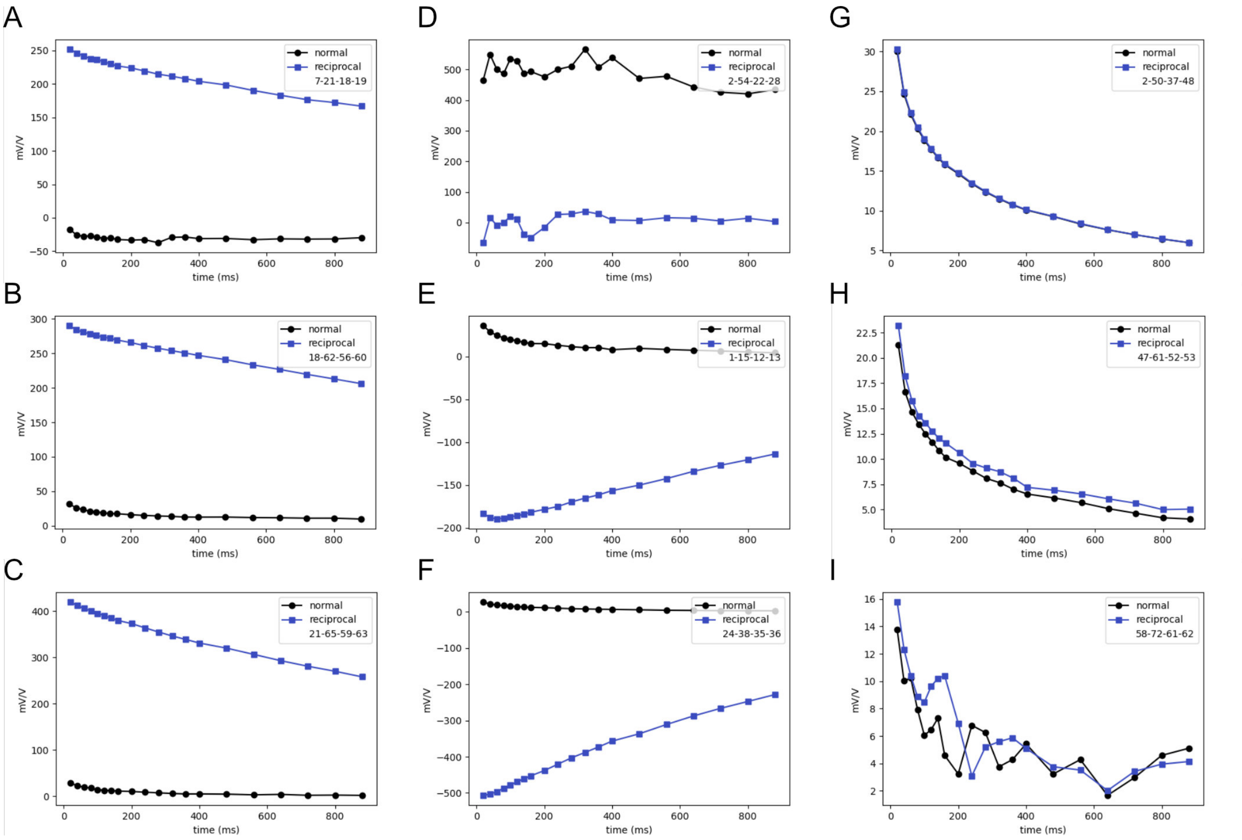

Figure 5. Normal and Reciprocal decay curves of the same quadrupoles. Column 1 (A-C) contains quadrupoles with a high positive offset (> 100 mV/V), column 2 (D-F) contains quadrupoles with a high negative offset (< -100 mV/V), and column 3 (G-I) contains quadrupoles with a small offset (between 1 and -1 mV/V).

ferent current distributions (Fig. 6). Further away from the injection dipole, the current density is lower, the effect of which is stronger in the reciprocal setting. Similarly, because of the short dipole distance for injection, the current density is high in this area but decreases more rapidly.

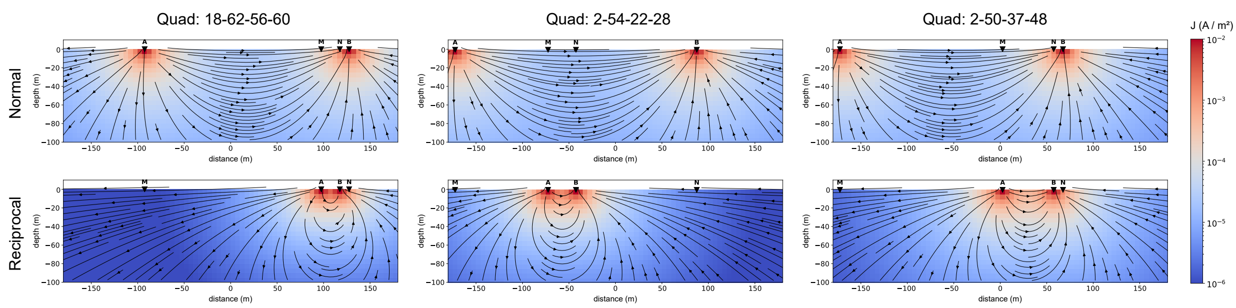

Figure 6. Current density simulated using the SimPEG framework Cockett et al. (2015) for the normal and reciprocal settings of three selected quadrupoles, corresponding to figure 5B,D,G.

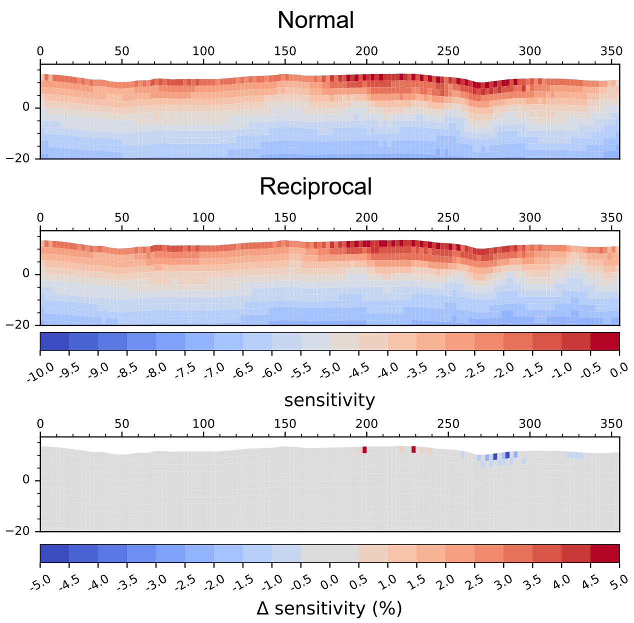

Figure 7. Cumulative sensitivity of the inversion model for the normal and reciprocal inversions, and the relative difference between the two.

3.2 Inversion

After removal of poor decay curves, the remaining datasets (normal and reciprocal) were transformed to phase shift φ using the CPA model, resulting in a conversion factor of -1.3 corresponding to the injection and measurement characteristics (Kemna, 2000; Thibaut et al., 2021). The inversion is well resolved in the upper 15 to 20 m (Fig. 7), as is expected from the data filtering step and the local hydrogeology. The inversion results are trimmed to an elevation of -10 m corresponding to a logarithmic normalized cumulative sensitivity level of approximately -5. The use of the reciprocal in the multigradient protocol does not seem to influence the inversion sensitivity, apart from some local effects in the top layer of the model; no differences are present in the inversion sensitivity (Fig. 7).

The complex conductivity σ^* is given by its real σ' and imaginary σ'' parts (Fig. 8). In both the normal and reciprocal, the real conductivity is low ($<$ 300 mS/m) in the upper 10 m with a thicker anomaly between 180 and 300 m on the profile. The real condctivity increases at depth. There is a small difference of 5 mS/m between normal and reciprocal (Fig. 8C) located at the end of the profile between 300 and 350 m. This difference is relatively weak (< 2 %), given the range of values for the real parameter. This small deviation is the results of the discrepancy in the observed

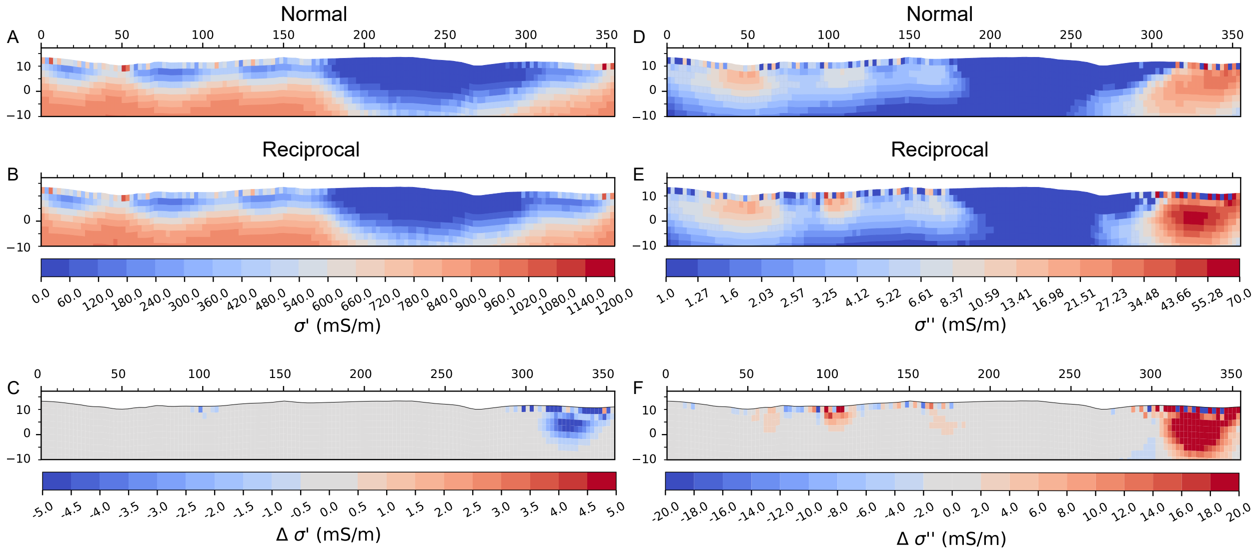

Figure 8. Inversions of the normal and reciprocal profile for the real part of the data (A & B), the imaginary part (D & E), and the absolute difference of the respective parameters (C & F), the difference is calculated relative to the reciprocal so a positive shift means a higher value for the reciprocal and vice versa.

apparent resistivity (Fig. 3). While there is a good match between N and R, a few readings have a larger difference. Knowing that $\sigma' = |\sigma| cos(-1.3) \approx |\sigma|$ and $\rho = 1/\sigma$ (Binley & Slater, 2020), a deviation in resistivity is expected to be mirrored in the real part of the conductivity. Interestingly, the discrepancy between normal and reciprocal data does not result in unstructured artefacts, but to a localized variations in real conductivity.

In the imaginary conductivity two anomalies are present: the first anomaly is present between 0 and 180 m, characterized by three connected clusters of increased conductivity, up to 20 mS/m. Visually, the anomaly is similar in both settings, as is confirmed by the difference profile where only small changes are present in this area. A second anomaly is present between 250 and 355 m with a plume-like geometry. Here, the difference is striking between normal and reciprocal, with a maximum of 30 mS/m for the normal and $>$70 mS/m for the reciprocal. In the difference image, the discrepancy between the two is localized between 300-355 m and has a spherical shape (Fig. 8F). The anomaly is much stronger for the reciprocal data than normal data, exceeding 20 mS/m or 100 $\%$.

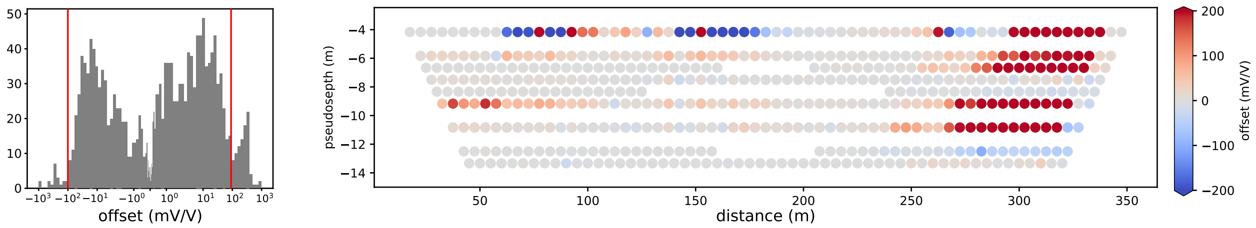

Figure 9. Average of the Normal-Reciprocal offset over 100 days. The panels correspond to figures **??**B, and 4.

3.3 Temporal stability of the anomaly

To ensure that the observed offset (Fig. 4) and the related anomaly in the inversion (Fig. 8F) are not the result of random noise, the analysis is repeated for the first 100 days of the monitoring campaign. If the monitoring results are consistent with the reference day, it indicates that the observed discrepancies are systematically present in the dataset, as is the case here (Fig. 9). The distribution of the average offset for each quadrupole (Fig. 9A) has a tail peak with increased offset between normal and reciprocal, at 100 mV/V, and is slightly more prominent for the time-lapse data than for the reference day. In the spatial distribution (Fig. 9B), no significant differences are present; the same clusters can be identified: a high anomaly between 280 and 340 m, and a cluster of negative offset in the first depth level associated with the negative IP effect.

Figure 10 is the time-lapse equivalent of Figure 5. Columns 1 and 2 contain quadrupoles with an offset of $>$100 mV/V, column 3 has a good match between normal and reciprocal with an offset $<$ 1 mV/V. A spread of the data is observable in the three categories, but is more prominent for the reciprocal measurements. This is to be expected as we collected the data using a multigradient protocol. The impact of noise is different under normal and reciprocal settings when working with a nested array. Reciprocal data have a large spacing between the potential electrodes and are hence more sensitive to noise. Quadrupoles where the chargeability does not cleanly decay also exhibit a larger spread on the data (Fig. 10D). This confirms that the offset is systematically present in the dataset and is reflected in the inversion. Figure 11 shows the anomaly between normal and reciprocal trough time, in the real and imaginary parts. In both cases the anomaly between 300-355 m remains present, but the geometry varies somewhat; this is to be expected given the observation of the spread in chargeability. In the imaginary part, the small anomaly increases through time.

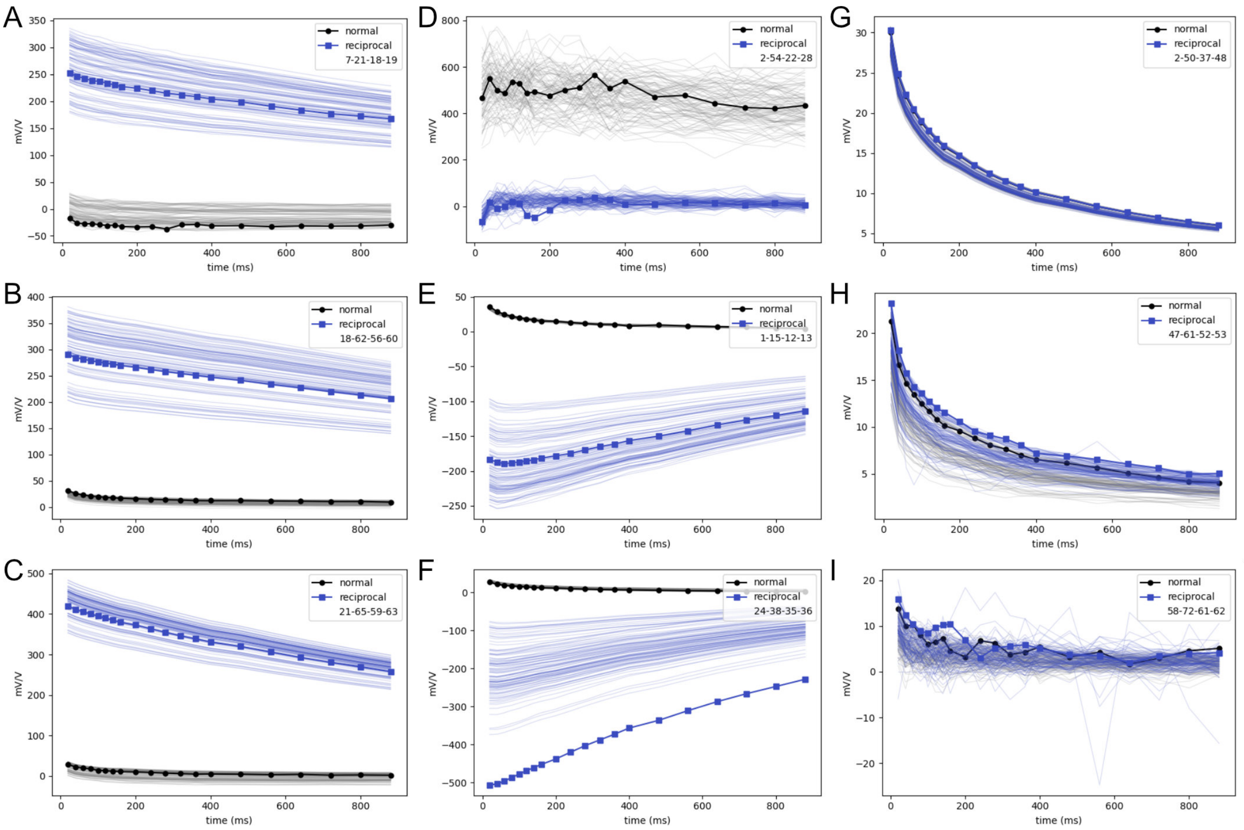

Figure 10. Decay curves of 100 analyzed dates, the quadrupoles correspond to the ones shown in Fig. 5 with the muted lines representing the subsequent measurements.

This can point to a natural alteration process as the measurements are carried out on an active geothermal field.

3.4 Neighbouring and Auxiliary Observations

On the field site, additional lines were collected before monitoring started. For a detailed description of profiles P2-P4 (Fig. 1), we refer to Vanhooren et al. (2025). Among all profiles, only profile 1, the monitoring line, has a significant IP anomaly. Profile 2 shows some minor IP anomaly, corresponding to an area of surface alteration, while the remainder of the profiles have no significant IP signal. The offset was computed for the neighbouring profiles (Fig. 12). In all three cases, the offset is centred more symmetrically around zero compared to profile 1, based on the histograms no significant offset can be identified. Profile 2 has a cluster of high and low offsets on the western side of the profile, between 0-100 m, intersecting with the anomaly between 0-180 m on profile 1. In contrast with profile 1, a clear consistent offset cannot be defined here based on the histogram.

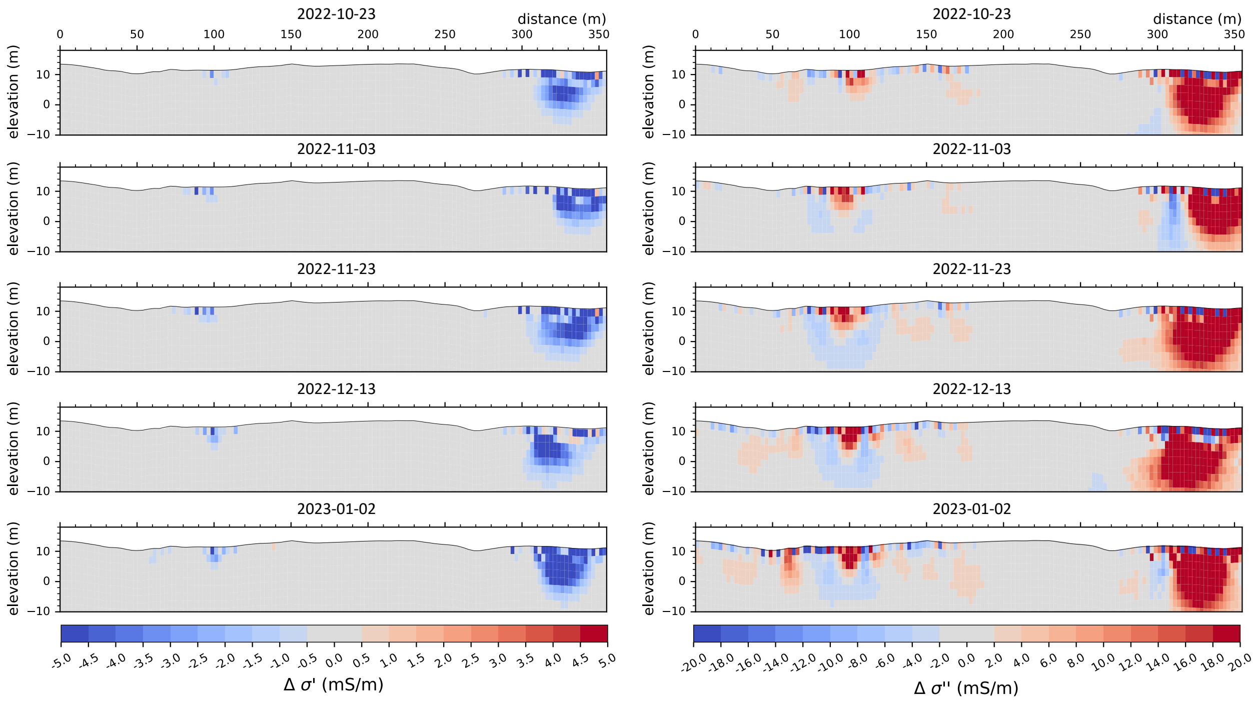

Figure 11. Timesteps of the anomaly in the real and imaginary conductivity as in Fig. 8C, F. A profile is shown every 20 days.

P4 crosses P1 around abscissa 270 m, but records no signal linked to the largest IP anomaly at the end of profile 1. Note that on all three profiles, an anomaly is noticable at a pseudodepth of -12.5 m, however, the offset is minimal, and further analysis is out of the scope of this contribution.

SP measurements were collected along the TDIP lines, anomalies are present in the active zones but also in the stable part, indicating upflow of hydrothermal fluids. The SP measurements of the monitoring line are shown in figure 13, a relative voltage increase is present in the area of the anomaly (300-355m). For a detailed signal description and interpretation, we refer to Vanhooren et al. (2025).

4 DISCUSSION

Before discussing the discrepancy, the IP anomaly itself needs to be considered in its geological context. Here we interpret the anomaly itself, for a more comprehensive description, we refer to the study of Vanhooren et al. (2025) where the geophysics (ERT, IP, SP) is jointly interpreted with temperature measurements and surface observations.

The inversion models (Fig. 8) reveal a prominent IP anomaly between 255 and 350 m on the

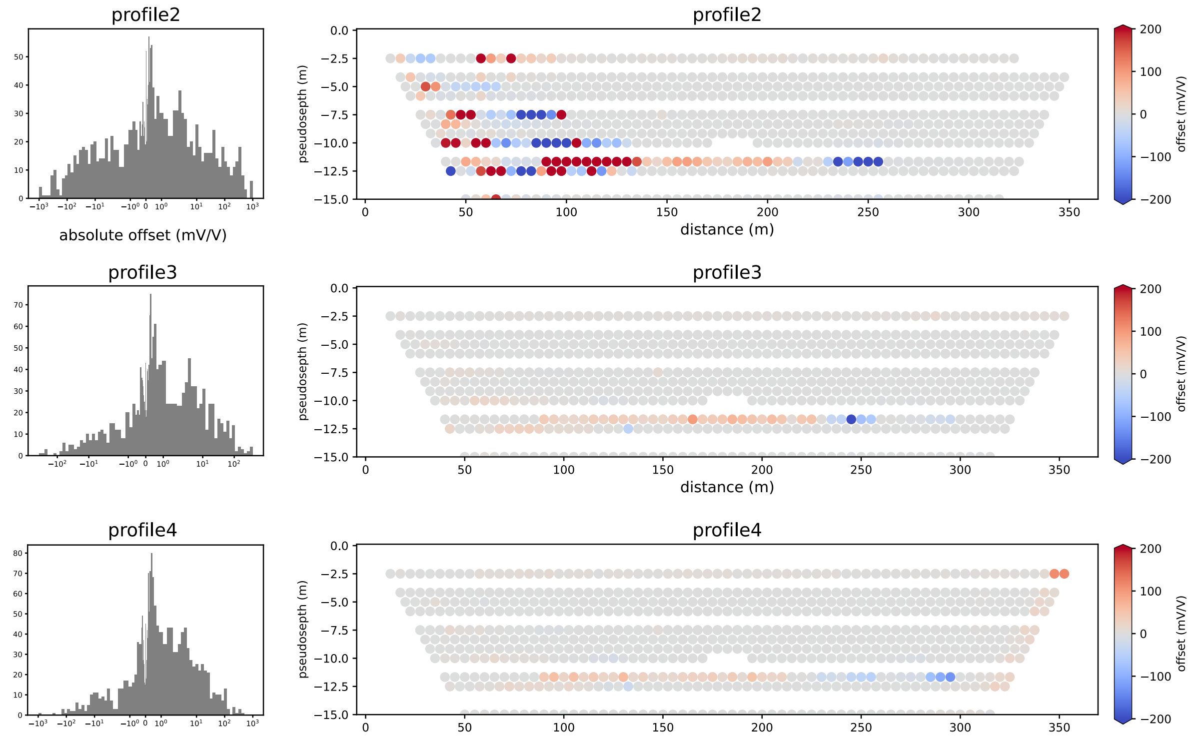

Figure 12. Offset distribution for profiles 2, 3, and 4 (see Fig. 1 for locations). A red line was drawn when the tail cluster could be identified.

profile, with a plume-like geometry reaching values of 30 mS/m in the normal and more than 70 mS/m in the reciprocal. This anomaly is significantly stronger than the one in the hydrothermally active zone (0-180 m), where clay minerals cause membrane polarization, giving values of 20 mS/m. The significant difference in absolute anomaly magnitude between the two areas indicates the presence of an additional polarization mechanism. While both areas exhibit EDL polarization of non-conductors, the southern zone shows a substantially stronger response attributed to the combined effect of membrane and electrode polarization. This intense IP anomaly, corroborated by the presence of a co-located SP anomaly and the geological context, supports the

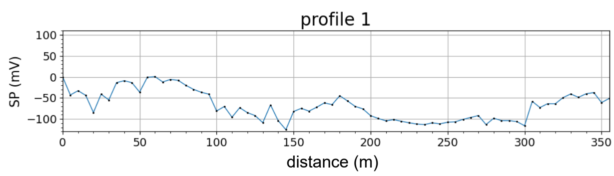

Figure 13. SP signal of profile 1, the oriëntation and electrode locations are the same as for the TDIP measurements.

interpretation of this zone as a hydrothermal seal composed of conductive minerals that prohibits fluid migration and surface alteration (Vanhooren et al., 2025).

4.1 Source of the Discrepancy

While electrode polarization explains the strength of the IP anomaly, it does not account for the systematic offset between normal and reciprocals. The offset is characterized by a consistently stronger response in the reciprocal, in a spatially confined zone (300-355m), which is consistently present over 100 consecutive days. The effect is much more prominent in the imaginary part (Fig. 8), which can be attributed to a scaling effect: since the polarizable part is several orders of magnitude smaller, subtle differences lead to strong relative variations that are better discernible. We consider five hypotheses for the source of this offset: 1) random noise, 2) polarization of the electrodes: when a stainless steel electrode is used to measure shortly after it was used for an injection, polarization of the electrode itself can occur. 3) sensitivity and signal strength: normal and reciprocal multigradient configurations have different sensitivity patterns and signal-to-noise ratios. The reciprocal setting, with larger potential electrode spacing, is inherently more sensitive to noise and could explain the offset. 4) systematic noise caused by stray currents of the nearby geothermal powerplant, and 5) a non-linear IP response which can be invoked under specific field conditions given the presence of clays and disseminated conductive minerals.

Rigorous data filtering using decay curve analysis, with the application of a RMSE of 75 % removes all spurious measurements with unexpected decay behaviour, ensuring they do not influence the analysis. The remaining dataset is inverted using a constant error model, the addition of an error model in the analysis allows for the data to be fitted within their noise level, accounting for any random noise. In addition, the consistency of the offset trough time, combined with the very localized nature of the anomaly, suggests a systematic effect is present.

Secondly, polarization effects and oxidation can occur around stainless steel electrodes. Upon careful survey design, stainless steel electrodes have been proven effective in IP surveys (Dahlin et al., 2002; Gündoğdu et al., 2022) with further minimization of the effect when current and potential electrodes are separated (Dahlin & Leroux, 2012). Using non-polarizable electrodes would eliminate the possibility of polarization effects. However, in a recent study Gündoğdu et al. (2022) reported that stainless steel electrodes provided more stable measurements than the non-polarizable $Cu - CuSO_4$ electrodes for monitoring. Given that the goal of the experiment is to monitor this site for several months, $Cu-CuSO_4$ electrodes were not an appropriate choice as the salt needs to remain saturated, requiring frequent maintenance, which is not practically feasible on this remote site. Electrode polarization was minimized when designing the survey; a delay on the measurements is used to account for coupling effects, and the protocol was sorted for minimal overlap/interference. Despite a careful design, electrode polarization can still be present, but it would be apparent when analysing the neighbouring datasets. All profiles were measured using the same protocol and in the same field conditions. If a problem was present in the sequence leading to electrode polarization, we would expect to observe it in all profiles, which is not the case (Fig. 12). In addition, we could expect this problem to occur at several locations or to be systematically linked to a bad electrode (bad coupling), which is not the case as contact resistance remained low during all the measurements.

Sensitivity differences are inherent to multigradient measurements and cannot be eliminated; the cumulative sensitivity of the inversion (Fig. 7) is quasi identical for both datasets, indicating that the inversion resolves the same volume. However, signal strength has an effect on the data as the reciprocal is more prone to noise, which can account for the small variation over time, but not for a systematic offset. Similarly to the polarization of electrodes, it would be expected that this effect is present in the neighbouring profiles as well, which is not the case.

The presence of systematic noise is more challenging to address, as a source of systematic noise would likely be systematically present in the monitoring dataset as well. In the field context, the nearby presence of the geothermal power plant is a likely source of systematic noise, such as stray currents. The classification of the signal as either a geological feature or systematic noise is not evident, as the SP signal can also be influenced by systematic noise. The ERT/TDIP data are corrected for the presence of an SP signal, but this correction can be subjected to error if the SP signal is fluctuating during the measurements. The fact that the discrepancy is consistent with time however suggests that the presence of a fluctuating SP signal alone cannot explain the discrepancy. Given the highly localized nature of the anomaly at the far end of the profile relative to the geothermal power plant, and the absence of discrepancy in the neighbouring profiles, we believe that the presence of systematic noise is not a convincing explanation. Regardless of the source of the discrepancy, the capacity to identify possible signal contamination is also of great scientific value.

The non-linear hypothesis is supported by several observations. Firstly, the current density simulations (Fig. 6) confirm that the reciprocal setting indeed produces a different, and locally higher, current distribution over the anomaly. The sign of the offset is consistent with Hallbauer-Zadorozhnaya et al. (2015), with a stronger IP response in the reciprocal, where the current density is higher. The area where the offset is present is interpreted as a hydrothermal seal containing a mixture of resistive oxides and semiconductive sulphides, where local heterogeneities can potentially be large enough to create an overpotential sufficient for nonlinear behaviour. The clay-rich environment causes the IP anomaly present between 0-180 m, dominated by membrane polarization, which behaves linearly at these current densities. The absence of a strong offset in this area suggests additional processes are in place.

The classification of this anomaly as either a systematic signal, related to non-linear responses, or systematic noise due to stray currents, is currently not possible and would require specified survey design and sample analysis. However, we illustrate that the reciprocal carries a lot of unused potential and can be used as an interpretation tool as well which is discussed further below.

4.2 Application potential

In this study, we performed TDIP measurements in a saline environment. For media dominated by electrochemical polarization, it is well known that the signal-to-noise ratio of IP signals drastically decreases at a salinity of 3000 mS/m (Weller et al., 2015). Below a pseudodepth of -15 m, virtually no data is accepted (Fig. 2). Note that the pseudosection depth is only an estimate, based on empirical assumptions (Dahlin & Zhou, 2006). In this regard, the sensitivity of the inversion is more reliable (Fig. 7), when applying a less conservative criterion, corresponding to a cumulative sensitivity of -5, we can consider the inversion reliable until an elevation of -10 m, corresponding to a depth of approximately -25 m below ground level. This is in accordance with previously reported depth of the saltwater interface by Sigurdsson (1986), putting it at -30 m b.g.l at the Reykjanes geothermal area. Since these numbers were reported in the 1980's before geothermal exploitation started, variations in depth and local differences are expected.

With this study, we want to encourage fellow scientists to not disregard IP as a tool in saline environments. In many cases, there is sufficient freshwater present to get good-quality IP readings (Cong-Thi et al., 2024). In northern and western Europe, fresh submarine groundwater discharge (SGD) has been widely reported, especially in the Baltic Sea (Hinsby et al., 2025) and also in the North Sea (Paepen et al., 2020). In the latter case, due to beach morphology, a zone of freshwater discharge is present on the lower beach, partially below the low-water line; in cases like this, TDIP measurement can potentially have sufficient signal-to-noise ratios to yield exploitable results. Other examples include small ocean islands, or atolls, where a large freshwater lens can develop in a high-permeability aquifer (Werner et al., 2017) and cases where seawater intrusion is prohibited by the presence of a low-permeability layer (Li et al., 2024).

The presented workflow relies on the offset between normal and reciprocal measurements to identify non-linear signals. The collection of reciprocals is common practice in DC resistivity surveys (e.g. Slater et al., 2000; Hermans et al., 2015; Tso et al., 2017) where it is applied to filter bad data and estimate an error model. In IP surveys, the quality of the data is generally assessed by decay curve analysis (DCA), Flores Orozco et al. (2018) even shows that the decays can also be utilized for filtering and error quantification of DC resistivity, eliminating the need for reciprocals. Given the nature of the field site, with low signal-to-noise-ratio at depth, this method is not appropriate as it would eliminate a significant portion of the resistivity measurements. By independently processing the normal and reciprocal data sets, a strong and systematic offset could be identified within en IP anomaly likely linked to the presence of iron sulfides and oxides, that we explained by a non-linear effect. In the specific profile illustrated here, the subsurface has a stronger response to the electric field in the reciprocal. Analogous to Hallbauer-Zadorozhnaya et al. (2015), by measuring the reciprocal of a multigradient protocol, the current density above the IP anomaly is stronger than in the normal protocol, offering a convincing argument for the non-linearity. Hence, we do think that the systematic analysis of reciprocals in IP surveys offers a widely accessible workflow to identify non-linearity without the need for laboratory analysis or specialized field equipment.

5 CONCLUSION

We present a Time Domain Induced Polarization dataset acquired in an active hydrothermal area. Independent analysis of the normal and reciprocal profiles reveals a spatially well-constrained anomaly where the two settings clearly deviate from each other, whilst in the remainder of the profile, there is a good match. This discrepancy is present in both the polarizable and non-polarizable parts of the signal, though it is much more prominent in the polarizable part, likely linked to scaling effects. It arises from a positive shift of the reciprocal decays relative to the normal, with an offset of 100 mV/V or more. Because the anomaly is consistently present in 100 consecutive days, random noise can be ruled out as the cause, which would be unlikely given the strict filtering criteria. Careful data acquisition and survey design minimize electrode polarization effects, since the neighboring measurements were made using the same configuration, electrode effects would be expected there as well, which is not the case. Thus, we can state that the observed signal likely represents a real subsurface anomaly rather than (measurement) artefacts. Whether the signal is related to a geological process or represents stray currents caused by human activities remains ambiguous. Given the geological context of the site, we deem a nonlinear response as a likely source of the discrepancy. The site is prone to strong alterations and other geothermal expressions, such as the development of a shallow seal containing (semi-)conductive minerals. Given that the anomaly is so localized and absent from other profiles, stray currents caused by electromagnetic noise are unlikely. However, in order to determine whether the measurement represents systematic noise or a systematic signal, field sampling and laboratory analysis is warranted. This study is part of a continuous ERT/TDIP experiment monitoring changes in volcanic and hydrothermal activity; hence survey design was optimized for continuous monitoring. In the future, this can be improved upon for the identification of nonlinear signals.

Here we present a workflow that is widely accessible. Reciprocal measurements are often made in geo-electric surveys, but mainly from a data-quality perspective. Here we argue for an additional purpose as an interpretation tool. When discrepancies like these are identified, neither the normal or reciprocal reflects the real distribution of the property in the subsurface, and should thus rather be used in a qualitative manner, whether it represents nonlinear processes or systematic noise. An additional advantage is that the method does not require advanced modelling techniques or the measurement of spectral data, making it suitable and easy to use for field surveys.

6 DATA AVAILABILITY

The monitoring data presented in this manuscript has been published in the Zenodo repository and is freely accessible at the following link: https://doi.org/10.5281/zenodo.15488867

7 ACKNOWLEDGMENTS

This manuscript is part of the ERupT project, funded by the Flanders Research Foundation (FWO), grant G037222N. We thank the colleagues for their help in coordinating the experiment and extend our gratitude to field operator HSOrka for allowing us to conduct our experiment on their site.

References

Archie, G. E., 1941. The electrical resistivity log as an aid in determining some reservoir characteristics, *Transactions AIME*, pp. 54–62.

Bigalke, J. & Junge, A., 1999. Using evidence of non-linear induced polarization for detecting extended ore mineralizations, *Geophysical Journal International*, **137**(2), 516–520.

Binley, A. & Slater, L., 2020. *Resistivity and Induced Polarization - Theory and Applications to the Near-Surface Earth*, cambridge university press.

Björnsson, S., Arnorsson, S., & Tomasson, J., 1970. Exploration of the reykianes thermal brine area, *Geothermics*, **2**, 1640–1650.

Bretaudeau, F., Dubois, F., Kassa, S. G. B., Coppo, N., Wawrzyniak, P., & Darnet, M., 2021.

Time-lapse resistivity imaging: Csem-data 3-d double-difference inversion and application to the reykjanes geothermal field, *Geophysical Journal International*, **226**, 1764–1782.

Caterina, D., Hermans, T., & Nguyen, F., 2014. Case studies of incorporation of prior information in electrical resistivity tomography: Comparison of different approaches, *Near Surface Geophysics*, **12**, 451–465.

Cockett, R., Kang, S., Heagy, L. J., Pidlisecky, A., & Oldenburg, D. W., 2015. Simpeg: An open source framework for simulation and gradient based parameter estimation in geophysical applications, *Computers & Geosciences*.

Cong-Thi, D., Dieu, L. P., Caterina, D., De Pauw, X., Thi, H. D., Ho, H. H., Nguyen, F., & Hermans, T., 2024. Quantifying salinity in heterogeneous coastal aquifers through ert and ip: Insights from laboratory and field investigations, *Journal of Contaminant Hydrology*, **262**, 104322.

Dahlin, T. & Leroux, V., 2012. Improvement in time-domain induced polarization data quality with multi-electrode systems by separating current and potential cables, *Near Surface Geophysics*, **10**(6), 545–565.

Dahlin, T. & Zhou, B., 2004. A numerical comparison of 2d resistivity imaging with 10 electrode arrays, *Geophysical Prospecting*, **52**, 379–398.

Dahlin, T. & Zhou, B., 2006. Multiple-gradient array measurements for multichannel 2d resistivity imaging, *Near Surface Geophysics*, **4**, 113–123.

Dahlin, T., Leroux, V., & Nissen, J., 2002. Measuring techniques in induced polarisation imaging, *Journal of Applied Geophysics*, **50**, 279–298.

Defourny, A., Nguyen, F., Collignon, A., Jobé, P., Dassargues, A., & Kremer, T., 2020. Induced polarization as a proxy for co2-rich groundwater detection—evidences from the ardennes, south-east of belgium, *Water*, **12**(5).

Evrard, M., Dumont, G., Hermans, T., Chouteau, M., Francis, O., Pirard, E., & Nguyen, F., 2018. Geophysical investigation of the pb–zn deposit of lontzen–poppelsberg, belgium, *Minerals*, **8**.

Flores-Orozco, A., Williams, K. H., Long, P. E., Hubbard, S. S., & Kemna, A., 2011. Using complex resistivity imaging to infer biogeochemical processes associated with bioremediation of an uranium-contaminated aquifer, *Journal of Geophysical Research: Biogeosciences*, **116**.

Flores Orozco, A., Williams, K. H., & Kemna, A., 2013. Time-lapse spectral induced polarization imaging of stimulated uranium bioremediation, *Near Surface Geophysics*, **11**(5), 531–544.

Flores Orozco, A., Gallistl, J., Bücker, M., & Williams, K. H., 2018. Decay curve analysis for data error quantification in time-domain induced polarization imaging, *GEOPHYSICS*, **83**(2), E75–E86.

Florsch, N., Camerlynck, C., & Maineult, A., 2026. Opinion note on nonlinearity in induced polarization, *Geophysical Journal International*, **244**(1), ggaf422.

Fowler, A. P., Zierenberg, R. A., Schiffman, P., Marks, N., & omar Fridleifsson, G., 2015. Evolution of fluid-rock interaction in the reykjanes geothermal system, iceland: Evidence from iceland deep drilling project core rn-17b, *Journal of Volcanology and Geothermal Research*, **302**, 47–63.

Fridleifsson, G. O., Elders, W. A., Zierenberg, R. A., Fowler, A. P., Weisenberger, T. B., Mesfin, K. G., Sigurdsson, O., Níelsson, S., Einarsson, G., Oskarsson, F., Gudnason, E., Tulinius, H., Hokstad, K., Benoit, G., Nono, F., Loggia, D., Parat, F., Cichy, S. B., Escobedo, D., & Mainprice, D., 2020. The iceland deep drilling project at reykjanes: Drilling into the root zone of a black smoker analog, *Journal of Volcanology and Geothermal Research*, **391**, 106435.

Fridriksson, T., Kristjánsson, B. R., Ármannsson, H., Margrétardóttir, E., Ólafsdóttir, S., & Chiodini, G., 2006. Co2 emissions and heat flow through soil, fumaroles, and steam heated mud pools at the reykjanes geothermal area, sw iceland, *Applied Geochemistry*, **21**, 1551–1569.

Ghorbani, A., Revil, A., Coperey, A., Ahmed, A. S., Roque, S., Heap, M. J., Grandis, H., & Viveiros, F., 2018. Complex conductivity of volcanic rocks and the geophysical mapping of alteration in volcanoes, *Journal of Volcanology and Geothermal Research*, **357**, 106–127.

Gündoğdu, N. Y., Demirci, , Özyildirim, , Aktarakçi, H., & Candansayar, M. E., 2022. Investigating the use of stainless steel electrodes with the ip method: A metallic ore deposit example, *Pure and Applied Geophysics*, **179**(1), 265–274.

Hallbauer-Zadorozhnaya, V., Santarato, G., & Abu Zeid, N., 2015. Non-linear behaviour of electrical parameters in porous, water-saturated rocks: a model to predict pore size distribution, *Geophysical Journal International*, **202**(2), 871–886.

Hallbauer-Zadorozhnaya, V. Y., Santarato, G., Zeid, N. A., & Bignardi, S., 2016. A non-linear induced polarization effect on transient electromagnetic soundings, *Journal of Applied Geophysics*, **133**, 16–24.

Hermans, T., Wildemeersch, S., Jamin, P., Orban, P., Brouyère, S., Dassargues, A., & Nguyen, F., 2015. Quantitative temperature monitoring of a heat tracing experiment using cross-borehole ert, *Geothermics*, **53**, 14–26.

Hermans, T., Maene, A., Caudron, C., & Vanhooren, L., 2026. Unsupervised data selection for focused time-lapse inversion in electrical resistivity tomography monitoring, *GEOPHYSICS*, accepted.

Hermans, T. J., 2014. *Integration of near-surface geophysical, geological and hydrogeological data with multiple-point geostatistics in alluvial aquifers*.

Hinsby, K., Scholten, J., Virtasalo, J., Szymczycha, B., Leth, J. O., Andersen, L. T., Ondracek, M., Tulstrup, J., Latacz, M., & Bannasch, R., 2025. Towards a digital information platform for locating and assessing environmental impacts of submarine groundwater discharge: Examples from the baltic sea, *Journal of Marine Science and Engineering*, **13**(3).

Kadko, D., Gronvold, K., & Butterfield, D., 2007. Application of radium isotopes to determine crustal residence times of hydrothermal fluids from two sites on the reykjanes peninsula, iceland, *Geochimica et Cosmochimica Acta*, **71**, 6019–6029.

Karlsdottir, R., Vilhjálmsson, A. M., & Árni Gudnason, E., 2020. Three dimensional inversion of magnetotelluric (mt) resistivity data from reykjanes high temperature field in sw iceland, *Journal of Volcanology and Geothermal Research*, **391**.

Kemna, A., 2000. *Tomographic inversion of complex resisitvity-theory and application.*.

Klein, J. & Shuey, R., 1978a. Nonlinear impedance of mineral-electrolyte interfaces; part i, pyrite, *Geophysics*, **43**(6), 1222–1234.

Klein, J. & Shuey, R., 1978b. Nonlinear impedance of mineral-electrolyte interfaces; part ii, galena, chalcopyrite, and graphite, *Geophysics*, **43**(6), 1235–1249.

LaBrecque, D. J., Miletto, M., Daily, W., Ramirez, A., & Owen, E., 1996. The effects of noise on Occam's inversion of resistivity tomography data, *Geophysics*, **61**(2), 538–548.

Lajaunie, M., Maurya, P. K., & Fiandaca, G., 2016. Comparison of Cole-Cole and Constant Phase Angle modeling in time-domain induced polarization, in *Proceedings of the 4th International Workshop on Induced Polarization (IP2016)*, Aarhus, Denmark.

Lesmes, D. P. & Frye, K. M., 2001. Influence of pore fluid chemistry on the complex conductivity and induced polarization responses of berea sandstone, *Journal of Geophysical Research: Solid Earth*, **106**(B3), 4079–4090.

Li, C., Gibbes, B., Liu, Y., Liu, X., & Zhang, C., 2024. Groundwater, salt and contaminant transport in a coastal aquifer system with a low-permeability layer in the intertidal zone, *Hydrological Processes*, **38**(5), e15149.

Lévy, L., Gibert, B., Sigmundsson, F., Flóvenz, O. G., Hersir, G. P., Briole, P., & Pezard, P. A., 2018. The role of smectites in the electrical conductivity of active hydrothermal systems: Electrical properties of core samples from krafla volcano, iceland, *Geophysical Journal International*, **215**, 1558–1582.

Marks, N., Schiffman, P., Zierenberg, R. A., Franzson, H., & o Fridleifsson, G., 2010. Hydrothermal alteration in the reykjanes geothermal system: Insights from iceland deep drilling program well rn-17, *Journal of Volcanology and Geothermal Research*, **189**, 172–190.

Oldenburg, D. W. & Li, Y., 1994. Subspace linear inverse method, *Inverse Problems*, **10**, 915–935.

Olhoeft, G., 1979. Nonlinear electrical properties, *Nonlinear behavior of molecules, atoms and ions in electric, magnetic or electromagnetic fields, Neel, L.(ed.), Elsevier Publishing Co., Amsterdam*, pp. 395–410.

Olhoeft, G., 1985. Low-frequency electrical properties, *Geophysics*, **50**(12), 2492–2503.

Paepen, M., Hanssens, D., Smedt, P. D., Walraevens, K., & Hermans, T., 2020. Combining resistivity and frequency domain electromagnetic methods to investigate submarine groundwater discharge in the littoral zone, *Hydrology and Earth System Sciences*, **24**, 3539–3555.

Paepen, M., Deleersnyder, W., Latte, S. D., Walraevens, K., & Hermans, T., 2022. Effect of groundwater extraction and artificial recharge on the geophysical footprints of fresh submarine groundwater discharge in the western belgian coastal area, *Water*, **14**.

Parasnis, D., 1988. Reciprocity theorems in geoelectric and geoelectromagnetic work, *Geoexploration*, **25**(3), 177–198.

Pelton, W. H., Wards, S. H., Hallof, P. G., Sills, W. R., & Nelson5, P. H., 1978. Mineral discrimination and removal of inductive coupling with multifrequency ip, *GEOPHYSICS*, **43**.

Revil, A. & Skold, M., 2011. Salinity dependence of spectral induced polarization in sands and sandstones, *Geophysical Journal International*, **187**(2), 813–824.

Revil, A., Hermitte, D., Spangenberg, E., & Cochemé, J. J., 2002. Electrical properties of zeolitized volcaniclastic materials, *Journal of Geophysical Research: Solid Earth*, **107**.

Revil, A., Florsch, N., & Mao, D., 2015. Induced polarization response of porous media with metallic particles — part 1: A theory for disseminated semiconductors, *GEOPHYSICS*, **80**.

Sigurdsson, F., 1986. Hydrogeology and groundwater on the reykjanes peninsula, *Jökull*, **36**, 11–29.

Slater, L., Binley, A., Daily, W., & Johnson, R., 2000. Cross-hole electrical imaging of a controlled saline tracer injection, *Journal of Applied Geophysics*, **44**, 85–102.

Slater, L. D. & Lesmes, D., 2002. Ip interpretation in environmental investigations, *Geophysics*, **67**(1), 77–88.

Slater, L. D., Choi, J., & Wu, Y., 2005. Electrical properties of iron-sand columns: Implications for induced polarization investigation and performance monitoring of iron-wall barriers, *Geophysics*, **70**(4), G87–G94.

Snarskii, A. A., Zorinets, D., Shamonin, M., & Kalita, V. M., 2019. Theoretical method for calculation of effective properties of composite materials with reconfigurable microstructure: Electric and magnetic phenomena, *Physica A: Statistical Mechanics and its Applications*, **535**, 122467.

Sæmundsson, K., Sigurgeirsson, M., & omar Fridleifsson, G., 2020. Geology and structure of the reykjanes volcanic system, iceland, *Journal of Volcanology and Geothermal Research*, **391**.

Thibaut, R., Kremer, T., Royen, A., Ngun, B. K., Nguyen, F., & Hermans, T., 2021. A new workflow to incorporate prior information in minimum gradient support (mgs) inversion of electrical resistivity and induced polarization data, *Journal of Applied Geophysics*, **187**.

Troiano, A., Isaia, R., Tramparulo, F., & Di Giuseppe, M., 2021. The pisciarelli main fumarole mechanisms reconstructed by electrical resistivity and induced polarization imaging, *Scientific Reports*, **11**(1), 18639.

Tso, C.-H. M., Kuras, O., Wilkinson, P. B., Uhlemann, S., Chambers, J. E., Meldrum, P. I., Graham, J., Sherlock, E. F., & Binley, A., 2017. Improved characterisation and modelling of measurement errors in electrical resistivity tomography (ert) surveys, *Journal of Applied Geophysics*, **146**, 103–119.

Ustra, A., Slater, L., Ntarlagiannis, D., & Elis, V., 2012. Spectral induced polarization (SIP) signatures of clayey soils containing toluene, *Near Surface Geophysics*, **10**(6), 503–515.

Vanhooren, L., Vrancken, E., Dekoninck, W., Flores-Orozco, A., Fontaine, O., Bergursson, B., Jonsdottir, K., Caudron, C., & Hermans, T., 2025. *Volcanica*.

Waxman, M. H. & Smits, L., 1968. Electrical conductivities in oil-bearing shaly sands, *Society of Petroleum Engineers Journal*, **8**(02), 107–122.

Weller, A., Zhang, Z., & Slater, L., 2015. High-salinity polarization of sandstones, *GEOPHYSICS*, **80**(3), D309–D318.

Weller, A., Zhang, Z., Slater, L., Kruschwitz, S., & Halisch, M., 2016. Induced polarization and pore radius—a discussion, *Geophysics*, **81**(5), D519–D526.

Werner, A. D., Sharp, H. K., Galvis, S. C., Post, V. E., & Sinclair, P., 2017. Hydrogeology and management of freshwater lenses on atoll islands: Review of current knowledge and research needs, *Journal of Hydrology*, **551**, 819–844, Investigation of Coastal Aquifers.

Zhdanov, M., 2008. Generalized effective-medium theory of induced polarization, *Geophysics*, **73**(5), F197–F211.